ADVANCED ENERGY MATERIALS
www.advenergymat.de

Ultrahigh Electron Thermal Conductivity in T-Graphene, Biphenylene, and Net-Graphene

Zhen Tong, Alessandro Pecchia, ChiYung Yam, Traian Dumitrică,* and Thomas Frauenheim**

Although isolated nonhexagonal carbon rings in graphene are associated with strain relaxation and curvature, dense and ordered arrangements of four-, five-, and eight-membered rings with strained carbon–carbon bonds can tile 2D planar layers. Using the Boltzmann transport equation formalism in combination with density functional theory calculations, how the presence of nonhexagonal rings impacts the thermal conductivity of three 2D carbon allotropes: T-graphene (four and eight rings), biphenylene (four, six, and eight rings), and net-graphene (four, six, and eight rings), is investigated. The phonon thermal conductivity (κ_{ph}), which captures three-phonon, four-phonon, and phonon–electron interactions, is significantly lowered with respect to pristine graphene. In compensation, the electron thermal conductivity (κ_e), which captures electron–phonon interactions, is enhanced to record high values, such that the room-temperature total thermal conductivity $\kappa_{total} = \kappa_{ph} + \kappa_e$ approaches the values of pristine graphene. 2D carbon allotropes could be of interest for applications requiring thermal energy transfer by a combination of diffusion of electrons and phonon vibrations.

1. Introduction

The discovery of buckminsterfullerene (C_{60}) molecule[1] was followed by the synthesis of other carbon allotropes,[2,3] including carbon nanotubes[4] and graphene.[5] While their structure is dominated by the presence of six-membered periodic carbon rings, nonhexagonal carbon rings are also encountered. For example, the C_{60} structure hosts 12 pentagons, which are responsible for the Gaussian curvature of the fullerene.[6] In carbon nanotubes and graphene, four-, five-, seven-, and eight-membered rings are encountered as extended[7] and mechanically-induced[8–10] five-five-seven-seven (Stone–Wales) and four-four-eight-eight defects, as well as chemical vapor deposition growth-induced grain boundaries.[11] The creation of curvature can be understood by viewing these rings as the cores of edge dislocations in the otherwise perfect hexagonal structure (cylindrical or flat).[10] Due to the extremely low bending rigidity combined with extremely high in-plane stiffness of graphene,[12,13] the extension in the out-of-plane dimension becomes an effective way to relax the core strain and bring the stiff C—C bonds closer to their preferred equilibrium value.

Theoretical explorations predicted that 2D carbon allotropes with regular nonhexagonal carbon rings can still be flat. For example, first-principles calculations[14–16] revealed stability for T-graphene, which comprises only tetrarings shown in **Figure 1**a. With the progress in materials synthesis, 2D carbon allotropes with non-hexagonal rings are now a reality. Notably, Fan et al.[17] and Liu et al.[18] reported successful growth of flat biphenylene and net-graphene, both comprising periodically arranged four-, six-, and eight-membered rings. As indicated in Figure 1a, these 2D carbon allotropes are significantly higher in energy ΔE than graphene. T-graphene is 0.52 eV per atom above graphene, while biphenylene and net-graphene have ΔE of 0.47 and 0.30 eV per atom, respectively. Nevertheless, finite-temperature structural relaxations of these allotropes to graphene in stress-free conditions must be considerably hindered by the large kinetic barriers for C—C bond rotations.[8,19]

Understanding the physical properties of 2D carbon allotropes, including mechanical,[20,21] electronic,[21,22] and optical[23] is a current focus, and some recently reports reveled many intriguing properties such as high-temperature superconductivity[24] and large lithium storage capacity.[17] In view of the ultrahigh thermal conductivity of graphene[25] of phononic

Z. Tong, C. Y. Yam, T. Frauenheim
Shenzhen JL Computational Science and Applied Research Institute
Shenzhen 518131, China
E-mail: tongzhen@csar.ac.cn
Z. Tong, C. Y. Yam, T. Frauenheim
Beijing Computational Science Research Center
Beijing 100193, China
A. Pecchia
CNR-ISMN
Via Salaria Km 29.300, Monterotondo, Rome 00017, Italy
T. Dumitrică
Department of Mechanical Engineering
University of Minnesota
Minnesota 55455, USA
E-mail: dtraian@me.umn.edu
T. Frauenheim
Bremen Center for Computational Materials Science
University of Bremen
2835 Bremen, Germany
E-mail: thomas.frauenheim@bccms.uni-bremen.de
The ORCID identification number(s) for the author(s) of this article can be found under https://doi.org/10.1002/aenm.202200657.

DOI: 10.1002/aenm.202200657

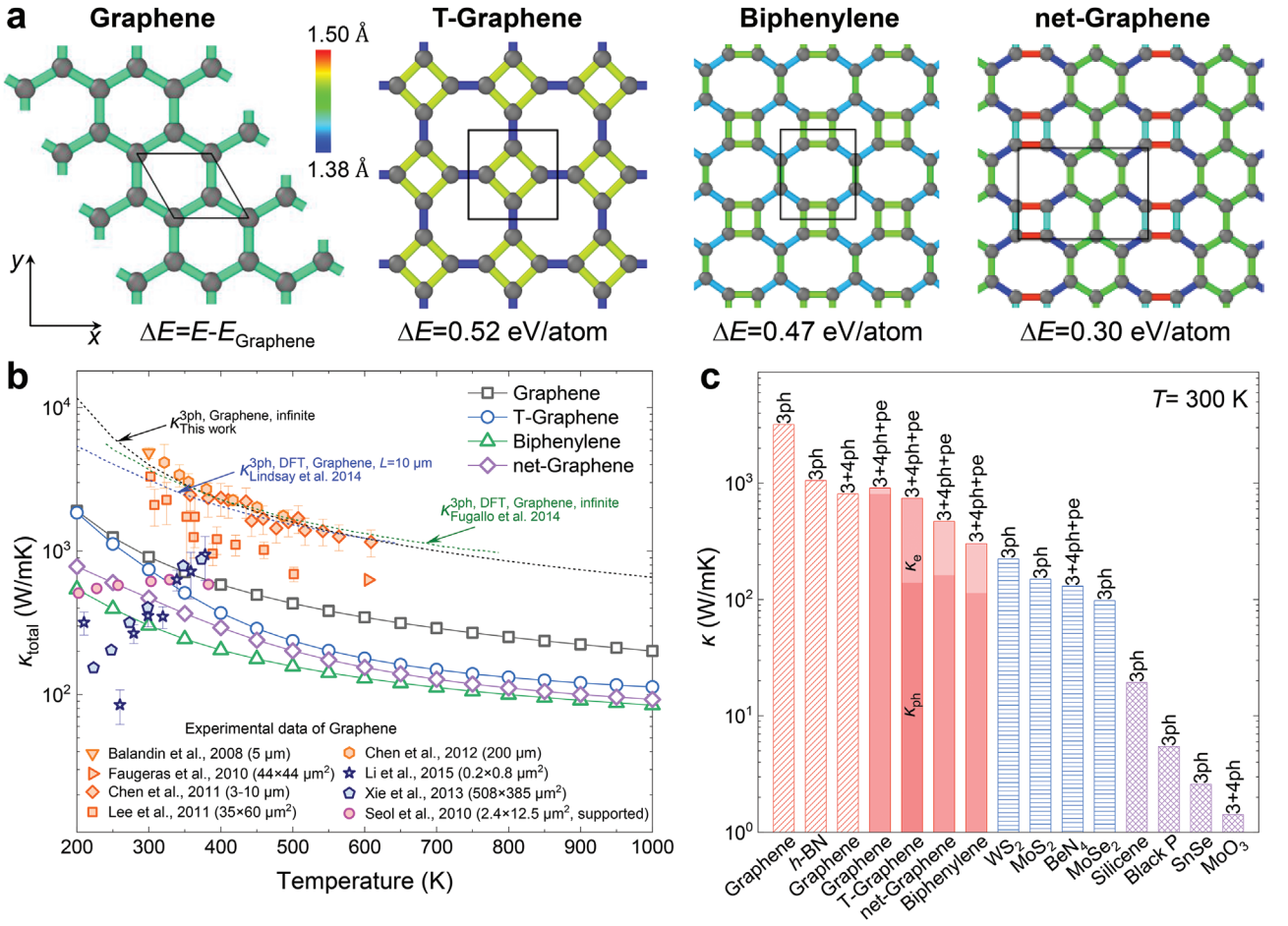

Figure 1. a) Computed crystal structures for graphene, T-graphene, biphenylene, and net-graphene. The color code shows the bonds lengths. The unit cells are indicated with dark line. ΔE is the total energy measured with respect to graphene. b) Computed $\kappa_{total} = \kappa_{ph} + \kappa_e$ versus T. Additionally, experimental thermal conductivity data for suspended (Balandin et al.,[25] Faugeras et al.,[37] Chen et al.,[38] Lee et al.,[39] Chen et al.,[40] Li et al.,[41] and Xie et al.[42]) and supported (Seol et al.[51]) graphene with different experimental sample size as well as the previous theoretical predictions of graphene (Lindsay et al.[45] and Fugallo et al.[46]) are provided for comparison. c) Thermal conductivity of single-layer 2D materials at $T = 300$ K. Literature data (theoretical) for graphene,[35,45] h-BN,[52] 2D WS_2 and MoS_2,[53] 2D $MoSe_2$,[53] 2D BeN_4,[34] silicene,[54] phosphorene,[55] SnSe,[56] and 2D MoO_3.[36] The label on top of the bars denotes 3ph only, 3+4ph, and 3+4ph+pe scattering events for computing κ_{ph}.

origin, the thermal properties are a particular focus. Without the out-of plane relaxations, the C—C bonds of the three 2D carbon allotropes are strained to different extents (C—C bonds in the 1.38–1.50 Å range) with respect to the bonding (C—C bonds 1.42 Å) of graphene shown in Figure 1a. The corresponding lattice constants of those 2D carbon allotropes are provided in Figure S1, Supporting Information. In strained bonds, anharmonicity effects[26,27] can decrease significantly the phonon thermal conductivity (κ_{ph}).[28–31]

In this work, we conduct a comprehensive ab initio calculation to consistently compare the phonon- and electron-based conduction of pristine graphene with that of the T-graphene, biphenylene, and net-graphene carbon allotropes. There is an established notion that thermal energy transport in 2D carbon materials is largely phonon-based[32] and that the negligible electron-based conduction can become important only under n-doping.[33,34] Contrary to this notion, here we find that in 2D carbon allotropes with nonhexagonal rings, the electron thermal conductivity (κ_e), as calculated by considering electron–phonon (el-ph) scatterings, is of central importance. The large κ_e compensates the drop in κ_{ph} which is calculated here by including not only the three-phonon (3ph) but also the four-phonon (4ph) and phonon–electron (pe) scatterings. The latter contribution is neglected by other approaches,[28,29] but recently it was shown to cause strong suppression of κ_{ph} in graphene,[35] MoO_3,[36] and BeN_4.[34]

2. Results and Discussions

2.1. κ_{total} of 2D Carbon Allotropes

Figure 1b plots the calculated $\kappa_{total} = \kappa_{ph} + \kappa_e$ (averaged within the in-plane directions) of graphene and the three 2D carbon allotropes in the temperature range of 200 to 1000 K. The temperature-dependent κ_{ph} and κ_e along x and y directions are shown in Figure S2, Supporting Information and the values at $T = 300$ K are given in Table S1, Supporting Information. The available experimental data for graphene, which is also shown, exhibits a large spread which may originate in both the sample variability (in terms of various defects and grain boundaries)

and the measurement technique. We note that Raman measurements[25,37–40] (orange solid dots) generally give larger thermal conductivity values than the thermal bridge methods[41,42] (navy solid dot) which are extended from the measurement of nanowire[43] and nanotubes.[44] Interestingly, the Raman data is in agreement with the graphene calculations which consider only 3ph scatterings[45,46] while the other measurements are instead in better agreement with the current calculations, which consider both 3ph and 4ph scatterings. It should be also noted that measurements of the thermal conductivity with the Raman method are subjected to rather large uncertaintinities[47] caused by the use of estimates of the light absorption coefficient and the temperature increase of the sample absorbing the light. Further, the method assumes that the temperature increase of the sample equals the temperature increase of the acoustic phonons, and uses this latter temperature increase to calculate the value of the thermal conductivity via the slope of the peak shift versus temperature shift. A theoretical work,[47] which has modeled the microscopic process of light energy absorption in graphene, uncovered severe overestimation of the thermal conductivity[25] by the Raman method, as also confirmed experimentally.[48] In this context, our result here further supports the critique of the Raman technique.[47]

It is well known that phonon (lattice vibration) is the major heat carrier in graphene and the electronic contribution can be neglected.[49] According to conventional wisdom, we expect a similar behavior in the sp^2 2D allotropes. Surprisingly, in spite of the strained C—C bonds, κ_{total} of the three carbon allotropes are rather similar with the value for graphene. For a broader view, in Figure 1c we place our calculation results in the context of other important 2D materials. It can be seen that κ_{total} at $T = 300$ K for the T-graphene, biphenylene, and net-graphene is in the high range, comparable to *h*-BN and larger than MoS_2. Interestingly, the recently predicted graphene-like borophene[50] displays a twofold higher thermal conductance than graphene. This reveals a weak ballistic thermal transport ability for 2D carbon allotropes compared to graphene-like borophene.

2.2. κ_{ph} and κ_e Components

To understand the high κ_{total} in 2D carbon allotropes, we analyze separately their κ_{ph} and κ_e components, **Figure 2**a), as well as their phononic and electronic band structures, Figure 2b,c, respectively. As expected, we find that κ_{total} of graphene is dominated by κ_{ph}, which is larger than in the other three 2D carbon allotropes. On the contrary, κ_e of the other three 2D carbon allotropes are above or close to their κ_{ph} components. We also note that the κ_e behavior is fully consistent with the electronic band structure of Figure 2c. In graphene and the electronic contribution can be neglected due to the almost zero electron density-of-states (DOS) originating from the Dirac point shown in Figure 2c at the Fermi level.[49] However, metallic features are observed in T-graphene, biphenylene, and net-graphene according to the electronic band dispersion crossover at the Fermi level shown in Figure 2c, hence the non-negligible electronic contribution to heat conduction.

We note in passing that by including 3+4ph+pe scatterings, which is the most complete scheme of phonon-limited scattering rate predictions based on ab initio calculations, our κ_{ph} calculations are surpassing the available literature data provided (red dot circles) in the left insets of Figure 2a. Specifically, we show κ_{ph}^{3+4ph} adopting the solution of Boltzmann transport equation (BTE) with the optimized Tersoff potential[58] for graphene,[35] κ_{ph}^{3ph} calculated from density functional theory (DFT) for T-graphene,[28] κ_{ph} calculated from the DFT with only 3ph scatterings[29] and the equilibrium molecular dynamics[30] (EMD) for biphenylene, and κ_{ph} by nonequilibrium EMD (NEMD) for net-graphene.[31] Overall, our calculations agree with the literature data, indicating the reliability of our implementations, and further allow for the following insights: i) The 4ph scattering effects induce a suppression $(\kappa_{ph}^{3ph}-\kappa_{ph}^{3+4ph})/\kappa_{ph}^{3ph}$ at $T = 300$ K by 79%, 78%, 51%, and 58% for graphene, T-graphene, biphenylene, and net-graphene, respectively. This indicates the importance of 4ph scatterings when computing the κ_{ph}. ii) The pe scatterings induce a further suppression $(\kappa_{ph}^{3+4ph}-\kappa_{ph}^{3+4ph+pe})/\kappa_{ph}^{3+4ph}$ at $T = 300$ K by 0.01%, 15%, 34%, and 3% for graphene, T-graphene, biphenylene, and net-graphene, respectively. This demonstrates the need for considering the pe interactions to predict κ_{ph}. iii) These two points are next supported by the data in the right inset of Figure 2a showing for each structure the magnitude of the 3ph, 4ph, and pe scattering rates. In particular, we note that the weak pe coupling behavior in graphene does not extend to the other three 2D allotropes.

2.3. Origin of High κ_e

Focusing on electron-based conduction, **Figure 3**a compares the calculated κ_e versus T for graphene, T-graphene, biphenylene and net-graphene. We can see that graphene has the smallest κ_e. At $T = 300$ K, see inset of Figure 3a, and the electronic contribution to heat conduction κ_e/κ_{total} in graphene is only of ≈10%. Remarkably, this contribution increases to 81%, 60%, and 66% in T-graphene, biphenylene, and net-graphene, respectively. The calculated electrical conductivity σ versus T plotted in Figure 3b displays a similar trend as κ_e versus T. For a broader view, we placed our predicted σ values in the context of typical metals[59] shown in the right inset of Figure 3b. T-graphene, biphenylene, and net-graphene show larger σ values than metals at $T = 300$ K, indicating their robust capability of electrical transport in potential electronic devices.

The σ calculations displayed in Figure 3b are confirming the weak electronic contribution to electron transport in graphene. We have compared our predictions with the measured σ of graphene as shown in Figure 3a. Similar to the thermal conductivity measurement in graphene, a large spread in the experiment data is also observed for σ. Our results overall locate the same order of the experimental data, indicating the reliability of our calculations. Our predictions in general further agree with the calculations using the Allen's model[63] (see Section S4, Supporting Information) as shown in Figure S3, Supporting Information, which obviously validates our implementation. For all four structures, we have also calculated their room-temperature intrinsic mobility $\mu = \sigma/ne$ (where e is the elementary charge and n is the charge carrier density). We obtained 0.22, 3.81, 1.22, and 1.51 (10^4 cm^2 V^{-1} s^{-1}) for graphene, T-graphene, biphenylene, and net-graphene, respectively. Due to the lowest electron density of states near the Fermi level (at the Dirac point), graphene has the smallest μ. The order of magnitude (10^4 cm^2 V^{-1} s^{-1})

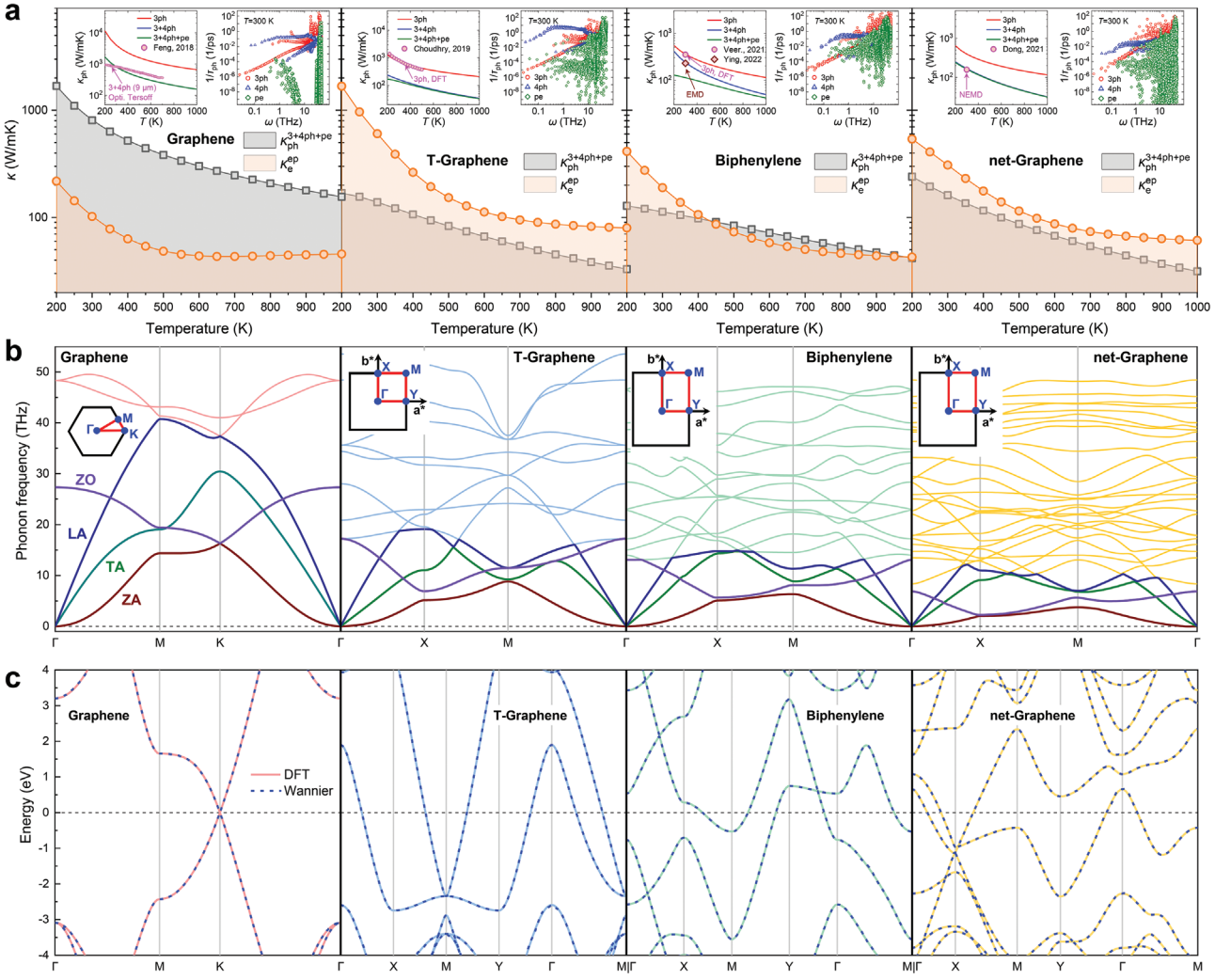

Figure 2. a) κ_{ph} and κ_e versus T, b) harmonic phonon dispersion, and c) electronic band structure from DFT calculations and Wannier interpolation[57] for graphene, T-graphene, biphenylene, and net-graphene. In (a), the left inset is the κ_{ph} attributed to different scattering events and the right inset is the scattering rates due to 3ph, 4ph, and pe interaction processes at $T = 300$ K. The most recently available literature data are provided for validation as marked in the left inset of (a) with: κ_{ph}^{3+4ph} for graphene,[35] κ_{ph}^{3ph} for T-graphene,[28] κ_{ph} calculated by only 3ph scatterings[29] and EMD[30] for biphenylene, and κ_{ph} by NEMD for net-graphene.[31] In (b), the TA, LA, ZA, and one transverse optical (ZO) phonon modes are labeled and the Brillouin zone are shown. In (c), the zero of energy is set to the Fermi level.

obtained for T-graphene, biphenylene, and net-graphene is close to what was reported for other 2D carbon allotropes.[64]

While our theoretical framework is able to clearly distinguish the κ_e and κ_{ph} components, in practice it is very difficult to directly measure them. Some promising experimental methods[65] have been developed for direct κ_{ph} measurements, such as alloying technique,[66] superconducting technique,[67] and magnetothermal technique[68,69] but they are either very complicated to conduct, or limited to extremely low T. The electrical conductivity can be accurately and easily obtained. The Lorenz ratio $L = \kappa_e/\sigma T$ is generally adopted to estimate the phonon thermal conductivity as $\kappa_{ph} = \kappa_{total} - L\sigma T$ in which L is generally assumed to be the Sommerfeld value $L_0 = 2.44 \times 10^{-8}\Omega WK^{-2}$.[59,70] We note that this approximation is inadequate especially at low temperatures ($T \ll T_D$, where T_D is Debye temperature) since L has large differences compared to L_0.[59] Indeed, in the inset of Figure 3b we observe the large deviation between L and L_0 in the 2D carbon allotropes, that is, $L < L_0$, indicating that using the Sommerfeld value in this method underestimates (overestimates) κ_{ph} (κ_e). Our result supports the violation of the Wiedemann–Franz law in 2D Dirac materials[71] because the ratio of electron thermal conductance and electric conductance is a chemical-potential-dependent quantity.

For all four structures we display their electron lifetime (τ_e), Figure 3c, and their velocity (v_F) and DOS (N_F) at the Fermi level, Figure 3d. Invoking the Drude's free electron model, these are key quantities for κ_e since $\kappa_e^{Drude} = (\pi^2/3k_B^2T)N_F v_F^2 \tau_e$.[59] We see that graphene has the largest τ_e compared to other allotropes, a result that is attributed the extremely weak el-ph coupling, as shown later in Figure 5d. However, the largest τ_e does not lead to largest κ_e (or σ). With its Dirac point is located at the Fermi level, graphene has an extremely small N_F, which leads

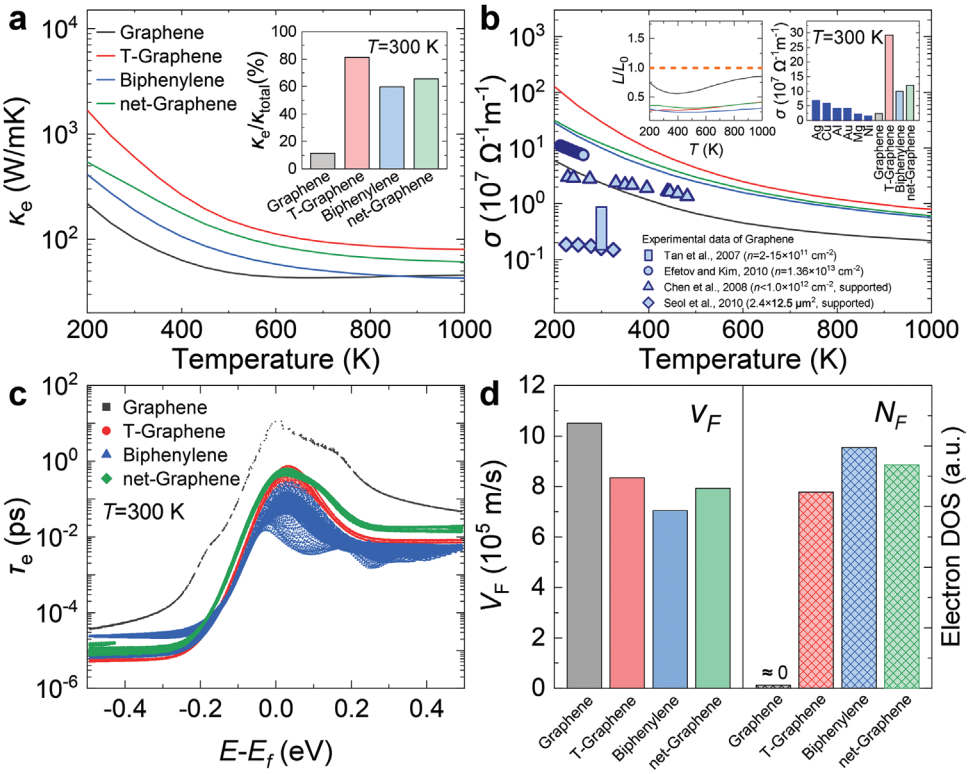

Figure 3. Comparison of a) κ_e versus T, (b) σ versus T, c) electron relaxation time, and d) Fermi velocity and electron DOS at Fermi level for graphene, T-graphene, biphenylene, and net-graphene. The inset of (a) is the ratio of κ_e/κ_{total} at $T = 300$ K. In (b), the left inset is the Lorenz ratio and the right inset is the electrical conductivity of some typical metals.[59] The experimental data[51,60–62] of σ in (b) are provided for comparison. Note: the σ is evaluated with single layer thickness of 0.334 nm.[51]

to a very small κ_e. T-graphene, biphenylene, and net-graphene have similar N_F values, which are much larger than graphene. Among them, we find that T-graphene has the largest κ_e (or σ) as it has the largest v_F and τ_e ($E - E_F$ within $k_BT \approx 0.026$ eV at 300 K). Our results and the insights uncovered here for T-graphene, biphenylene, and net-graphene could also be shared with other theoretically predicted 2D carbon allotropes displaying metallic character, such as penta-graphene, α-graphene, γ-graphene, Ψ-graphene, and pop-graphene.[3,31,64]

2.4. Origin of Low κ_{ph}

To understand the reasons behind lowering κ_{ph} in the 2D allotropes, as detailed for example in **Figure 4**a, we have carried a detailed comparison of the intrinsic phonon properties. The BTE derived κ_{ph}, see Equation (6), is conditioned by the volumetric heat capacity C_v, group velocity v_g, and relaxation time τ. By analyzing Figure 4b–d, where we have separately plotted these quantities for all four structures, we can see that all C_v, v_g, and τ contribute to the lowering of κ_{ph} with respect to graphene. First, we see that the C_v of graphene is much larger than that of T-graphene, biphenylene, and net-graphene, Figure 4b. Second, we find that the graphene has the largest v_g, a result which is more clear using the average $\langle v_g \rangle$ shown in the inset of Figure 4c. Note that since the κ_{ph} of all graphene allotropes is mainly attributed to the phonon modes less than 20 THz (mainly acoustic modes) shown in the inset of Figure 4a, in Figure 4c we have plotted the v_g of the acoustic modes only. Third, we find a distinct enhancement of the phonon scatterings in T-graphene, biphenylene, and net-graphene compared to graphene. On one hand, in graphene the normal phonon scattering rates are one to two orders of magnitude larger than the Umklapp phonon scattering rates shown in Figure 4d. This indicates a hydrodynamic phonon transport regime where the phonon transport is much less dissipative, leading to extraordinary large κ_{ph}.[72] On the other hand, in T-graphene, biphenylene, and net-graphene, we find in Figure 4d that the normal and Umklapp phonon scattering rates are at comparable levels at 300 K. This indicates the breakdown of hydrodynamic phonon transport (dominant in graphene) and a significant increase in dissipation.

Focusing next on the anharmonic effects, we find that all the important indicators concur to an enhancement of anharmonicity in T-graphene, biphenylene, and net-graphene. In Figure 4e we first find that compared to graphene there is a significant increase of phonon DOS for T-graphene, biphenylene, and net-graphene in 1–10 THz. Hence, less phonon interactions can occur in graphene. Second, in Figure 4f the Grüneisen parameter,[73] which is a measure of the anharmonicity, is smallest in graphene. Third, in Figure 4g we see that the phonon phase space reflecting all available phonon scattering processes for simultaneously satisfying the energy and momentum conservation in graphene is much smaller than that in T-graphene, biphenylene, and net-graphene. Forth, the

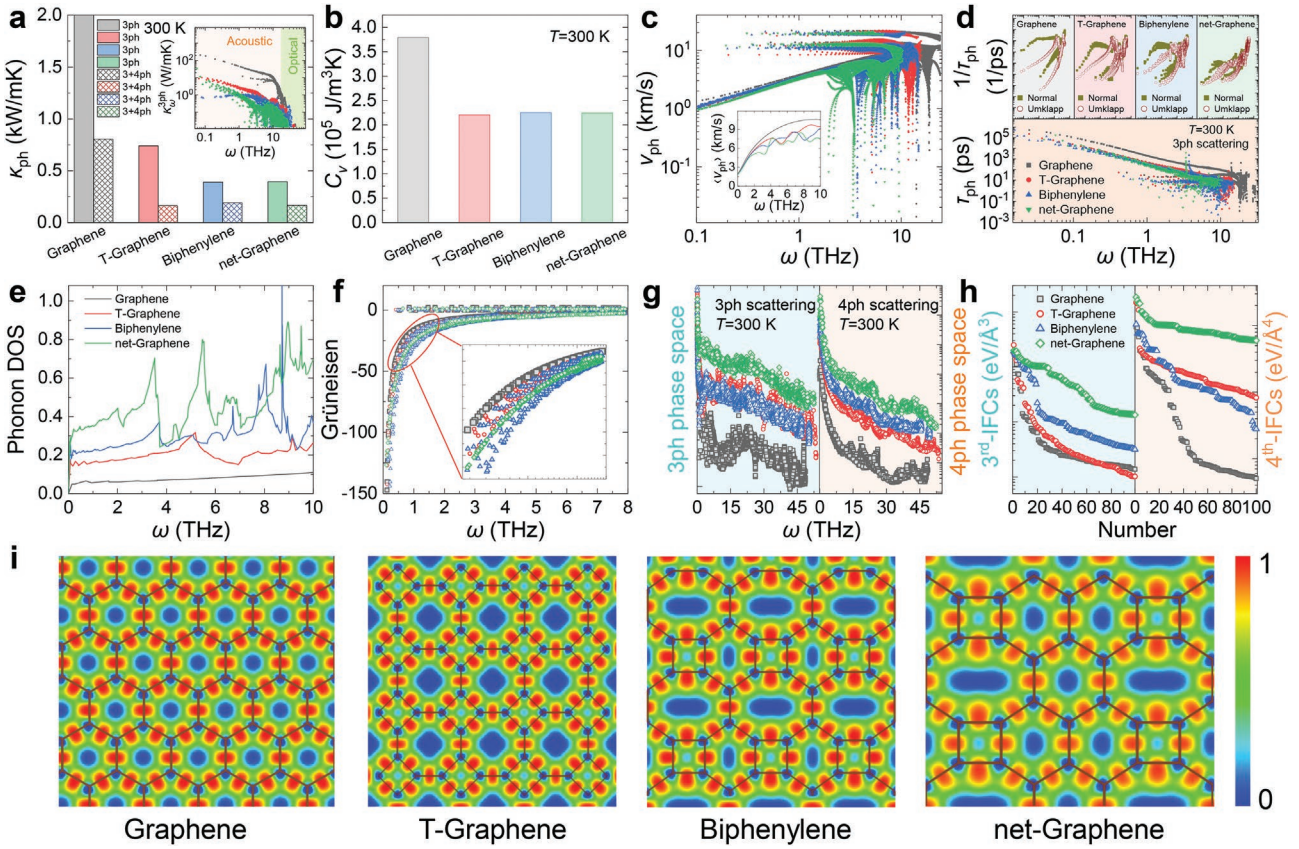

Figure 4. The comparison of a) κ_{ph}^{3ph} and κ_{ph}^{3+4ph} at $T = 300$ K, b) volumetric heat capacity at $T = 300$ K, c) phonon group velocity, d) phonon scattering rates from normal and Umklapp processes as well as the lifetime due to 3ph scatterings at $T = 300$ K, e) phonon DOS, f) Grüneisen parameter, g) phase space of 3ph and 4ph scattering events, h) the strength of 100 largest third- and fourth-IFCs matrix elements, and i) the ELF for graphene, T-graphene, biphenylene, and net-graphene. The inset of (a) is the spectral $\kappa_{ph}^{3ph}(\omega)$ at $T = 300$ K. The inset of (c) is the average group velocity. The inset of (f) is the Grüneisen parameter in the range of ≈1–2 THz. The ELF is visualized by using VESTA package.[74] Note: the representation of the color in (a–h) is gray for graphene, red for T-graphene, blue for biphenylene, and green for net-graphene, respectively.

anharmonic force constants of Figure 4h show that graphene has the smallest strength of the third and fourth order interatomic force constants (IFCs, Φ).

The strong anharmonicity displayed by T-graphene, biphenylene, and net-graphene in comparison with graphene originates in changes of the covalent bonding of strained bonds in reduced crystal symmetry environment. In Figure 4i, we characterize bonding with the electron localization function (ELF).[75,76] The position where the electron is localized has a high ELF value. As expected, ELF is largest at the center of all C—C bonds, indicating the dominance of covalent bonding in the 2D carbon allotropes. We can further observe that while in graphene, the distribution of ELF is symmetric with respect to the C—C bond axis, evident deviations are visible in T-graphene, biphenylene, and net-graphene. In the latter structures, ELF indicates that electrons spread toward the center of the larger eight-membered and six-membered rings and away from the center of the smaller four-membered rings. We interpret these ELF changes as a shift in sp^2 bonding caused by electrostatic repulsion, which spills the electronic charge from the smaller into the larger neighboring rings.

The ZA modes are known to be very important in the phonon transport in 2D materials.[32,51] We investigate their contribution to κ_{ph} arising from 3ph, 4ph and pe scatterings. In graphene, **Figure 5**a, we can see that the relative contribution of the ZA branch to κ_{ph} is reduced from 80% with only 3ph scattering to 30% after including 4ph scattering. Further including pe scatterings gives minor changes. As shown in Figure 5b, the reduction of κ_{ph}^{3+4ph} is caused by the enhancement of the 4ph scattering rates of ZA modes which are 3 to 4 orders larger than the 3ph scattering rates. These results do not follow the general rule of bulk materials that 4ph scattering is important only in strongly anharmonic materials.[77,78] The behavior obtained in graphene is attributed to the reflection symmetry selection rule, which is unique to 2D materials. Previous works[51,79] showed that reflection symmetry of graphene (or any 2D crystal) requires that the nth order anharmonic IFCs vanish: $\Phi^{l_1 b_1 \ldots l_n b_n}_{\alpha_1 \ldots \alpha_n} = 0$ when the number of out-of-plane components in the string $\alpha_1 \ldots \alpha_n$ is odd. This leads to a selection rule that forbids any n-phonon scattering process involving an odd number of flexural (out-of-plane) modes. Therefore, the three-ZA (ZA+ZA → ZA) scattering processes are forbidden. This means that the major 3ph scattering phase space for ZA modes is eliminated and the ZA modes are the major heat carriers accounted for by κ_{ph}^{3ph}. However, for 4ph scatterings, the four-ZA processes ZA+ZA→ZA+ZA and ZA→ZA+ZA+ZA are allowed. There is abundant 4ph scatterings for ZA modes, leading to

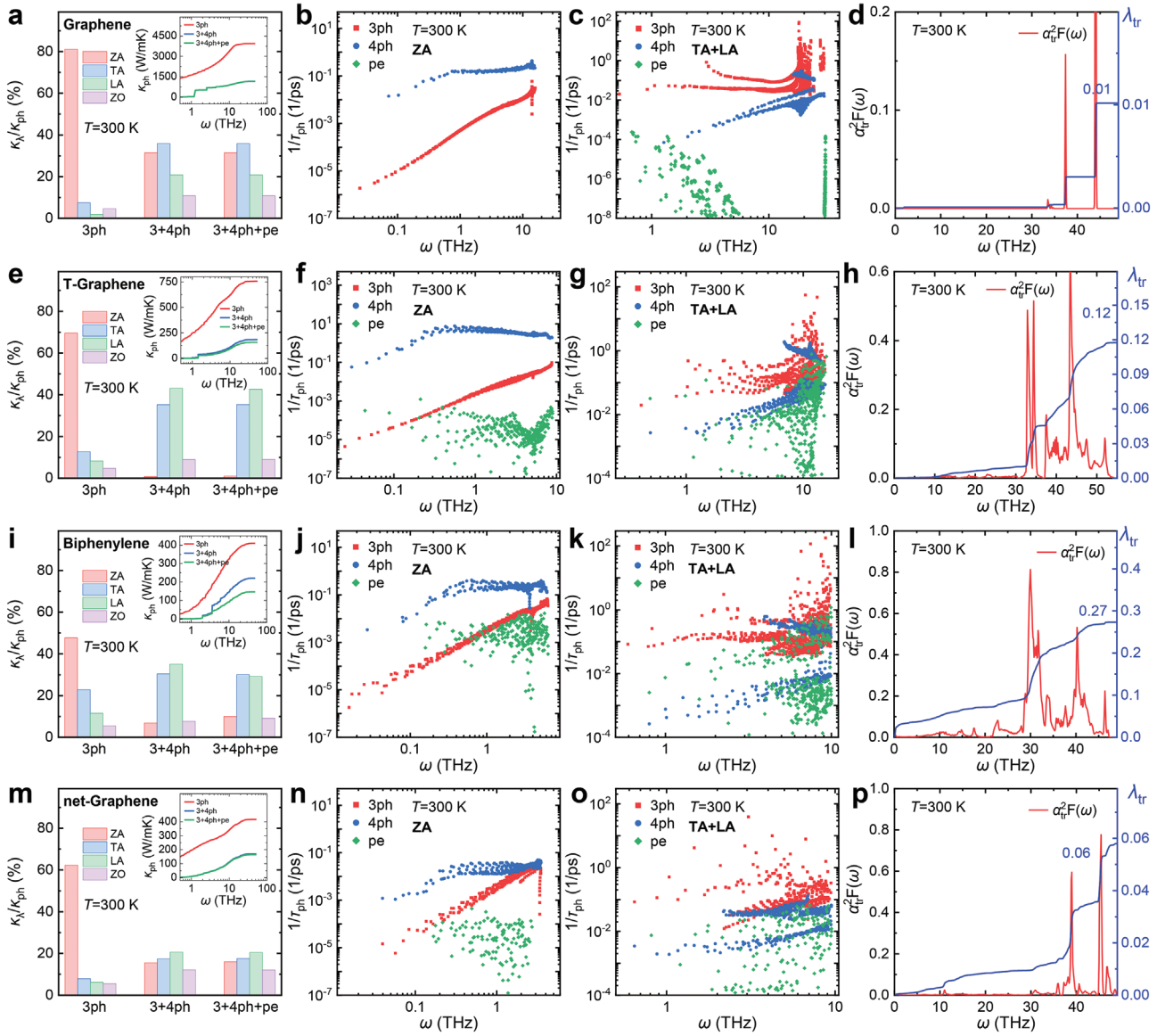

Figure 5. a) The normalized contribution of all acoustic modes and ZO modes to κ_{ph} attributed to 3ph, 3+4ph and 3+4ph+pe interactions, in which the inset is the accumulated κ_{ph} with respect to phonon frequency ω, b,c) 3ph, 4ph, and pe scatterings for all acoustic modes, and d) the Eliashberg spectral function $\alpha^2_{tr}F$ and transport el-ph coupling strength λ_{tr} at $T = 300$ K for graphene. The corresponding contents are fore–h) T-graphene, i–l) bipheylene, and (m–p) net-graphene.

the suppression of κ_{ph}^{3+4ph}. The ZA modes behave similarly in T-graphene, biphenylene, and net-graphene, where we can see significant suppression of κ_{ph}^{3+4ph} in Figure 5e,i,m as well as extremely large 4ph scattering rates in Figure 5f,j,n.

A different trend to the contribution to κ_{ph} is found for the TA and LA modes, Figure 5a,e,i,m. For these modes, a large percentage of 4ph processes than 3ph processes are forbidden, as shown in Figure 5c,g,k,o. In addition, from the inset of Figure 5a,e,i,m, we can see that the pe scattering effect on the κ_{ph} is relative small in graphene, T-graphene, and net-graphene but it is strong in biphenylene. The transport el-ph coupling strength λ_{tr} = 0.27 (see definition in Section S5, Supporting Information) for biphenylene shown in Figure 5l is larger than that of 0.01 for graphene in Figure 5d, 0.12 for T-graphene in Figure 5h, and 0.06 in Figure 5p for net-graphene, indicating the stronger el-ph coupling in biphenylene than other 2D carbon allotropes.

3. Conclusion

In conclusion, using the Boltzmann transport equation formalism in combination with density functional theory calculations, we uncovered 2D carbon allotropes with both electron-based and phonon-based thermal conduction. Although electron-based thermal conduction is small in graphene, it is ultrahigh in 2D carbon allotropes with non-hexagonal rings. Phonon-based conduction remains important, although the effect is deteriorated by

the anharmonicity effects caused by the changes in C—C bonding resulted from strain and lattice symmetry changes. The electron-based conduction compensates for the κ_{ph} decrease and renders large κ_{total} for T-graphene, biphenylene, and net-graphene, close to those of graphene, h-BN and MoS_2, which exhibit phonon-based thermal conduction. Other theoretically predicted 2D carbon allotropes, such as penta-graphene, α-graphene, γ-graphene, Ψ-graphene, and pop-graphene, display metallic character, and thus could share the impressive attributes uncovered here for T-graphene, biphenylene, and net-graphene. 2D carbon allotropes may contribute to realization of the next-generation technologies requiring nanostructures with ability to transfer of thermal energy by a combination of diffusion of electrons and phonon vibrations.

4. Experimental Section

Electronic Thermal Conductivity and Electrical Conductivity: By solving the BTE of electron,[80] the electrical conductivity tensor ($\sigma^{\alpha\beta}$) and electronic thermal conductivity tensor ($\kappa_e^{\alpha\beta}$) can be obtained as

$$\begin{cases} \sigma^{\alpha\beta} = L_{EE}^{\alpha\beta}, \\ \kappa_e^{\alpha\beta} = -\left(L_{TT}^{\alpha\beta} - \frac{L_{TE}^{\alpha\beta} L_{ET}^{\alpha\beta}}{L_{EE}^{\alpha\beta}} \right) \end{cases} \quad (1)$$

in which the coefficients are

$$L_{EE}^{\alpha\beta} = -\frac{e^2 n_s}{N_k V} \sum_{ik} \frac{\partial f_{ik}^0}{\partial \varepsilon_{ik}} v_{ik}^{\alpha} v_{ik}^{\beta} \tau_{ik}^{ep} \quad (2)$$

$$L_{ET}^{\alpha\beta} = -\frac{e n_s}{N_k V T} \sum_{ik} (\varepsilon_{ik} - \mu) \frac{\partial f_{ik}^0}{\partial \varepsilon_{ik}} v_{ik}^{\alpha} v_{ik}^{\beta} \tau_{ik}^{ep} \quad (3)$$

$$L_{TE}^{\alpha\beta} = -\frac{e n_s}{N_k V} \sum_{ik} (\varepsilon_{ik} - \mu) \frac{\partial f_{ik}^0}{\partial \varepsilon_{ik}} v_{ik}^{\alpha} v_{ik}^{\beta} \tau_{ik}^{ep} \quad (4)$$

$$L_{TT}^{\alpha\beta} = -\frac{n_s}{N_k V T} \sum_{ik} (\varepsilon_{ik} - \mu)^2 \frac{\partial f_{ik}^0}{\partial \varepsilon_{ik}} v_{ik}^{\alpha} v_{ik}^{\beta} \tau_{ik}^{ep} \quad (5)$$

where e is the elementary charge, n_s is the number of electrons per state, V is the volume of the unit cell, N_k the total number of **k**-points sampled in the first Brillouin zone, T is the temperature, f_{ik}^0 is the electron distribution function, $\mathbf{v}_{ik} = \frac{1}{\hbar} \frac{\partial \varepsilon_{ik}}{\partial \mathbf{k}}$ is the electron velocity, α and β denotes the directional component. The summation in these three equations was over all the electrons enumerated using electronic wave vector **k** and band index i. μ is the chemical potential. τ_{ik}^{ep} is the electron lifetime (or relaxation time). It should be noted that only the el-ph scattering rates ($1/\tau_{ik}^{ep}$) were considered in computing the κ_e. The expression of $1/\tau_{ik}^{ep}$ can be found in Section S1, Supporting Information.

Phononic Thermal Conductivity: Solving the BTE of phonon combined with the Fourier's law of heat conduction, the phonon thermal conductivity tensor ($\kappa_p^{\alpha\beta}$) can be written as a summation over all phonon modes $\lambda = (\mathbf{q}, \nu)$ of polarization ν, wave vector **q** and frequency ω_λ as

$$\kappa_p^{\alpha\beta} = \frac{1}{N_q} \sum_{\lambda} c_\lambda v_{\lambda,\alpha} v_{\lambda,\beta} \tau_\lambda^p \quad (6)$$

where α and β are indexing the Cartesian directions, N_q is the total number of **q**-points sampled in the first Brillouin zone, while c_λ, v_λ, and τ_λ^p denote the volumetric heat capacity, phonon group velocity, and phonon lifetime (or relaxation time), respectively. Note that $c_\lambda = (\hbar\omega_\lambda / V)(\partial n_\lambda^0 / \partial T)$, where n_λ^0 is the Bose–Einstein distribution function and V the volume of the primitive cell, and $v_{\lambda,\alpha} = \partial\omega_\lambda / \partial q_\alpha$. The phonon scattering rate ($1/\tau_\lambda^p$) is a summation of the phonon–phonon ($1/\tau_\lambda^{pp}$), pe ($1/\tau_\lambda^{pe}$), phonon–impurity ($1/\tau_\lambda^{im}$), phonon–isotope ($1/\tau_\lambda^{iso}$), and phonon–grain boundary ($1/\tau_\lambda^{gb}$) scattering rates. Here, the κ_p of tr-BeN_4 based on ab initio computed $1/\tau_\lambda^{pp}$ with 3ph and 4ph scatterings as well as $1/\tau_\lambda^{pe}$ scattering rates are predicted, which can be summed using Matthiessen's rule[80] with $1/\tau_\lambda^p = 1/\tau_\lambda^{3ph} + 1/\tau_\lambda^{4ph} + 1/\tau_\lambda^{pe}$. The detailed expressions of $1/\tau_\lambda^{3ph}$, $1/\tau_\lambda^{4ph}$, and $1/\tau_\lambda^{pe}$ can be found in Section S2, Supporting Information.

Ab Initio Computational Details: The DFT and density functional perturbation theory (DFPT) calculations were carried using the VASP[81] package with Perdew–Burke–Ernzerhof exchange and correlation functional.[82] The 3ph scattering rates were calculated using ShengBTE[73] and the 4ph scattering rates were computed using an in-house code.[36,77,83] The el-ph coupling matrix were calculated using DFPT with norm-conserving pseudopotentials[84] with generalized gradient approximation[82] exchange and correlation functional as implemented in QUANTUM ESPRESSO.[85] They were initially obtained on coarse electron and phonon wave vector grids and then implemented to finer grids using the maximally localized Wannier functions basis as implemented in the el-ph Wannier (EPW)[86,87] to obtain the el-ph scatterings for computing κ_e and κ_{ph}. Importantly, an in-house modified EPW code[70,88,89]was used to predict the el-ph coupling scattering rates in order to compute the huge dense **k**- and **q**-points more efficiently. The simulation parameters and computational details are provided in Section S3, Supporting Information.

Supporting Information

Supporting Information is available from the Wiley Online Library or from the author.

Acknowledgements

The authors thank Dr. Shouhang Li for valuable discussions. Simulations were performed at the Tianhe2-JK of Beijing Computational Science Research Center. Z.T. acknowledges the support by National Natural Science Foundation (No. 52106068), China Postdoctoral Science Foundation (No. 2020M680127), Guangdong Basic and Applied Basic Research Foundation (Nos. 2020A1515110838 and 2021A1515011688), and Shenzhen Science and Technology Program (No. RCBS20200714114919142). T.F. acknowledges support from DFG FR-2833/7 and National Natural Science Foundation of China (No. U1930402).

Conflict of Interest

The authors declare no conflict of interest.

Data Availability Statement

The data that support the findings of this study are available from the corresponding author upon reasonable request.

Keywords

2D materials, ab initio calculations, Boltzmann transport equation, carbon allotropes, electron thermal conductivity

Received: February 24, 2022
Revised: April 3, 2022
Published online: May 10, 2022

[1] H. W. Kroto, J. R. Heath, S. C. O'Brien, R. F. Curl, R. E. Smalley, *Nature* **1985**, *318*, 162.
[2] A. Hirsch, *Nat. Mater.* **2010**, *9*, 868.

[3] A. N. Enyashin, A. L. Ivanovskii, *Phys. Status Solidi B* **2011**, *248*, 1879.
[4] S. Iijima, *Nature* **1991**, *354*, 56.
[5] K. S. Novoselov, *Science* **2004**, *306*, 666.
[6] H. Terrones, A. Mackay, *Carbon* **1992**, *30*, 1251.
[7] J. Liu, H. Dai, J. H. Hafner, D. T. Colbert, R. E. Smalley, S. J. Tans, C. Dekker, *Nature* **1997**, *385*, 780.
[8] T. Dumitrică, M. Hua, B. I. Yakobson, *Proc. Natl. Acad. Sci. U. S. A.* **2006**, *103*, 6105.
[9] D.-B. Zhang, R. D. James, T. Dumitrică, *The Journal of Chemical Physics* **2009**, *130*, 071101.
[10] H. F. Bettinger, T. Dumitrică, G. E. Scuseria, B. I. Yakobson, *Phys. Rev. B* **2002**, *65*, 041406.
[11] P. Y. Huang, C. S. Ruiz-Vargas, A. M. van der Zande, W. S. Whitney, M. P. Levendorf, J. W. Kevek, S. Garg, J. S. Alden, C. J. Hustedt, Y. Zhu, J. Park, P. L. McEuen, D. A. Muller, *Nature* **2011**, *469*, 389.
[12] D.-B. Zhang, E. Akatyeva, T. Dumitrică, *Phys. Rev. Lett.* **2011**, *106*, 255503.
[13] I. Nikiforov, E. Dontsova, R. D. James, T. Dumitrică, *Phys. Rev. B* **2014**, *89*, 155437.
[14] Y. Liu, G. Wang, Q. Huang, L. Guo, X. Chen, *Phys. Rev. Lett.* **2012**, *108*, 225505.
[15] B. G. Kim, J. Y. Jo, H. S. Sim, *Phys. Rev. Lett.* **2013**, *110*, 029601.
[16] H. Huang, Y. Li, Z. Liu, J. Wu, W. Duan, *Phys. Rev. Lett.* **2013**, *110*, 029603.
[17] Q. Fan, L. Yan, M. W. Tripp, S. R. Kachel, M. Chen, A. S. Foster, U. Koert, P. Liljeroth, J. M. Gottfried, *Science* **2021**, *372*, 852.
[18] M. Liu, M. Liu, L. She, Z. Zha, J. Pan, S. Li, T. Li, Y. He, Z. Cai, J. Wang, Y. Zheng, X. Qiu, D. Zhong, *Nat. Commun.* **2017**, *8*, 14924.
[19] T. Dumitrică, B. I. Yakobson, *Appl. Phys. Lett.* **2004**, *84*, 2775.
[20] R. Majidi, *Theor. Chem. Acc.* **2017**, *136*, 109.
[21] Y. Luo, C. Ren, Y. Xu, J. Yu, S. Wang, M. Sun, *Sci. Rep.* **2021**, *11*, 19008.
[22] M. A. Hudspeth, B. W. Whitman, V. Barone, J. E. Peralta, *ACS Nano* **2010**, *4*, 4565.
[23] A. Bafekry, M. Faraji, M. M. Fadlallah, H. R. Jappor, S. Karbasizadeh, M. Ghergherehchi, D. Gogova, *J. Phys.: Condens. Matter* **2022**, *34*, 015001.
[24] Y.-T. Kang, C. Lu, F. Yang, D.-X. Yao, *Phys. Rev. B* **2019**, *99*, 184506.
[25] A. A. Balandin, S. Ghosh, W. Bao, I. Calizo, D. Teweldebrhan, F. Miao, C. N. Lau, *Nano Lett.* **2008**, *8*, 902.
[26] J. Al-Ghalith, Y. Ni, T. Dumitrică, *Phys. Chem. Chem. Phys.* **2016**, *18*, 9888.
[27] Z. Tong, A. Pecchia, C. Yam, T. Dumitrică, T. Frauenheim, *Adv. Sci.* **2021**, *8*, 2101624.
[28] U. Choudhry, S. Yue, B. Liao, *Phys. Rev. B* **2019**, *100*, 165401.
[29] H. P. Veeravenkata, *Carbon* **2021**, *183*, 893.
[30] P. Ying, T. Liang, Y. Du, J. Zhang, X. Zeng, Z. Zhong, *Int. J. Heat Mass Transfer* **2022**, *183*, 122060.
[31] H. Dong, Z. Zhang, Z. Feng, J. Kang, D. Wu, Q. Wang, J. Li, R. Su, *J. Mater. Res. Technol.* **2021**, *11*, 1982.
[32] X. Gu, Y. Wei, X. Yin, B. Li, R. Yang, *Rev. Mod. Phys.* **2018**, *90*, 041002.
[33] P. Rosenzweig, H. Karakachian, D. Marchenko, K. Küster, U. Starke, *Phys. Rev. Lett.* **2020**, *125*, 176403.
[34] Z. Tong, A. Pecchia, C. Yam, H. Bao, T. Dumitrică, T. Frauenheim, *Adv. Funct. Mater.* **2022**, *32*, 2111556.
[35] T. Feng, X. Ruan, *Phys. Rev. B* **2018**, *97*, 045202.
[36] Z. Tong, T. Dumitrică, T. Frauenheim, *Nano Lett.* **2021**, *21*, 4351.
[37] C. Faugeras, B. Faugeras, M. Orlita, M. Potemski, R. R. Nair, A. K. Geim, *ACS Nano* **2010**, *4*, 1889.
[38] S. Chen, A. L. Moore, W. Cai, J. W. Suk, J. An, C. Mishra, C. Amos, C. W. Magnuson, J. Kang, L. Shi, R. S. Ruoff, *ACS Nano* **2011**, *5*, 321.
[39] J.-U. Lee, D. Yoon, H. Kim, S. W. Lee, H. Cheong, *Phys. Rev. B* **2011**, *83*, 081419.
[40] S. Chen, Q. Wu, C. Mishra, J. Kang, H. Zhang, K. Cho, W. Cai, A. A. Balandin, R. S. Ruoff, *Nat. Mater.* **2012**, *11*, 203.
[41] Q.-Y. Li, K. Takahashi, H. Ago, X. Zhang, T. Ikuta, T. Nishiyama, K. Kawahara, *J. Appl. Phys.* **2015**, *117*, 065102.
[42] H. Xie, L. Chen, W. Yu, B. Wang, *Appl. Phys. Lett.* **2013**, *102*, 111911.
[43] D. Li, Y. Wu, P. Kim, *Appl. Phys. Lett.* **2003**, *83*, 2934.
[44] P. Kim, L. Shi, A. Majumdar, P. L. McEuen, *Phys. Rev. Lett.* **2001**, *87*, 215502.
[45] L. Lindsay, W. Li, J. Carrete, N. Mingo, D. A. Broido, T. L. Reinecke, *Phys. Rev. B* **2014**, *89*, 155426.
[46] G. Fugallo, A. Cepellotti, L. Paulatto, M. Lazzeri, N. Marzari, F. Mauri, *Nano Lett.* **2014**, *14*, 6109.
[47] A. K. Vallabhaneni, D. Singh, H. Bao, J. Murthy, X. Ruan, *Phys. Rev. B* **2016**, *93*, 125432.
[48] S. Sullivan, A. Vallabhaneni, I. Kholmanov, X. Ruan, J. Murthy, L. Shi, *Nano Lett.* **2017**, *17*, 2049.
[49] R. Prasher, *Science* **2010**, *328*, 185.
[50] J. He, D. Li, Y. Ying, C. Feng, J. He, C. Zhong, H. Zhou, P. Zhou, G. Zhang, *npj Comput. Mater.* **2019**, *5*, 47.
[51] J. H. Seol, I. Jo, A. L. Moore, L. Lindsay, Z. H. Aitken, M. T. Pettes, X. Li, Z. Yao, R. Huang, D. Broido, N. Mingo, R. S. Ruoff, L. Shi, *Science* **2010**, *328*, 213.
[52] A. Cepellotti, *Nat. Commun.* **2015**, *6*, 6400.
[53] X. Gu, R. Yang, *Appl. Phys. Lett.* **2014**, *105*, 131903.
[54] X. Gu, R. Yang, *J. Appl. Phys.* **2015**, *117*, 025102.
[55] L. Zhu, G. Zhang, B. Li, *Phys. Rev. B* **2014**, *90*, 214302.
[56] G. Qin, Z. Qin, W.-Z. Fang, L.-C. Zhang, S.-Y. Yue, Q.-B. Yan, M. Hu, G. Su, *Nanoscale* **2016**, *8*, 11306.
[57] A. A. Mostofi, J. R. Yates, Y.-S. Lee, I. Souza, D. Vanderbilt, N. Marzari, *Comput. Phys. Commun.* **2008**, *178*, 685.
[58] L. Lindsay, D. A. Broido, *Phys. Rev. B* **2010**, *81*, 205441.
[59] (Ed: T. M. Tritt), *Thermal Conductivity: Theory, Properties, and Applications*, Kluwer Academic/Plenum Publishers, New York **2004**.
[60] Y.-W. Tan, Y. Zhang, K. Bolotin, Y. Zhao, S. Adam, E. H. Hwang, S. Das Sarma, H. L. Stormer, P. Kim, *Phys. Rev. Lett.* **2007**, *99*, 246803.
[61] D. K. Efetov, P. Kim, *Phys. Rev. Lett.* **2010**, *105*, 256805.
[62] J.-H. Chen, C. Jang, S. Xiao, M. Ishigami, M. S. Fuhrer, *Nat. Nanotechnol.* **2008**, *3*, 206.
[63] P. B. Allen, *Phys. Rev. B* **1978**, *17*, 3725.
[64] J. Xi, D. Wang, Y. Yi, Z. Shuai, *J. Chem. Phys.* **2014**, *141*, 034704.
[65] W. H. Butler, R. K. Williams, *Phys. Rev. B* **1978**, *18*, 6483.
[66] R. K. Williams, D. W. Yarbrough, J. W. Masey, T. K. Holder, R. S. Graves, *J. Appl. Phys.* **1981**, *52*, 5167.
[67] P. M. Rowell, K. A. G. Mendelssohn, *Proc. R. Soc. Lond., Ser. A* **1960**, *254*, 542.
[68] H. N. D. Lang, H. V. Kempen, P. Wyder, *J. Phys. F Met. Phys.* **1978**, *8*, L39.
[69] M. Yao, M. Zebarjadi, C. P. Opeil, *J. Appl. Phys.* **2017**, *122*, 135111.
[70] S. Li, Z. Tong, X. Zhang, H. Bao, *Phys. Rev. B* **2020**, *102*, 174306.
[71] H. Zhou, Y. Cai, G. Zhang, Y.-W. Zhang, *Phys. Rev. B* **2016**, *94*, 045423.
[72] S. Lee, D. Broido, K. Esfarjani, G. Chen, *Nat. Commun.* **2015**, *6*, 6290.
[73] W. Li, J. Carrete, N. A. Katcho, N. Mingo, *Comput. Phys. Commun.* **2014**, *185*, 1747.
[74] K. Momma, F. Izumi, *J. Appl. Crystallogr.* **2011**, *44*, 1272.
[75] B. Silvi, A. Savin, *Nature* **1994**, *371*, 683.
[76] X. Wu, V. Varshney, J. Lee, T. Zhang, J. L. Wohlwend, A. K. Roy, T. Luo, *Nano Lett.* **2016**, *16*, 3925.
[77] T. Feng, X. Ruan, *Phys. Rev. B* **2016**, *93*, 045202.
[78] T. Feng, L. Lindsay, X. Ruan, *Phys. Rev. B* **2017**, *96*, 161201.
[79] L. Lindsay, D. A. Broido, N. Mingo, *Phys. Rev. B* **2011**, *83*, 235428.
[80] G. D. Mahan, *Many-Particle Physics*, 3 Ed., Kluwer Academic/Plenum Publishers, New York **2000**.
[81] G. Kresse, J. Hafner, *Phys. Rev. B* **1993**, *47*, 558.
[82] J. P. Perdew, K. Burke, M. Ernzerhof, *Phys. Rev. Lett.* **1996**, *77*, 3865.

[83] Z. Tong, X. Yang, T. Feng, H. Bao, X. Ruan, *Phys. Rev. B* **2020**, *101*, 125416.
[84] N. Troullier, J. L. Martins, *Phys. Rev. B* **1991**, *43*, 1993.
[85] P. Giannozzi, S. Baroni, N. Bonini, M. Calandra, R. Car, C. Cavazzoni, D. Ceresoli, G. L. Chiarotti, M. Cococcioni, I. Dabo, A. Dal Corso, S. de Gironcoli, S. Fabris, G. Fratesi, R. Gebauer, U. Gerstmann, C. Gougoussis, A. Kokalj, M. Lazzeri, L. Martin-Samos, N. Marzari, F. Mauri, R. Mazzarello, S. Paolini, A. Pasquarello, L. Paulatto, C. Sbraccia, S. Scandolo, G. Sclauzero, A. P. Seitsonen, et al., *J. Phys.: Condens. Matter* **2009**, *21*, 395502.
[86] J. Noffsinger, F. Giustino, B. D. Malone, C.-H. Park, S. G. Louie, M. L. Cohen, *Comput. Phys. Commun.* **2010**, *181*, 2140.
[87] S. Poncé, E. Margine, C. Verdi, F. Giustino, *Comput. Phys. Commun.* **2016**, *209*, 116.
[88] Z. Tong, H. Bao, *Int. J. Heat Mass Transfer* **2018**, *117*, 972.
[89] Z. Tong, S. Li, X. Ruan, H. Bao, *Phys. Rev. B* **2019**, *100*, 144306.